Volume 1 | Number 1 | Jan 2013 | Pages 1–100

Journal of
Materials Chemistry A

Materials for energy and sustainability
www.rsc.org/materialsA

Li⁺

ROYAL SOCIETY
OF CHEMISTRY

ROYAL SOCIETY
OF CHEMISTRY

www.rsc.org/materialsA

Journal Name

Bubble-Template-Assisted Synthesis of Hollow Fullerene-Like MoS₂ Nanocages as a Lithium Ion Battery Anode Material

Xiaoxia Zuo,[a, †] Kun Chang,*[ab, †] Jing Zhao,[c] Zhengzheng Xie,[a] Hongwei Tang,[a] Bao Li,[a] Zhaorong Chang*[a]

Inorganic fullerene (IF)-like structured materials have attracted considerable attention for electrochemical energy storage and conversion. In this report, we describe a facile method of synthesizing IF-MoS₂ hollow structures with a diameter of ~100 nm by a facile solution-phase reduction process to obtain a hollow MoSₓ precursor under ambient pressures before subsequent annealing of the material at high temperatures to form IF-MoS₂ nanocages. TEM images at different reaction stages reveal the hollow structure spontaneously arising in the novel "close-edge" nanocages under the assistance of ammonia cation bubble template. When evaluated as an anode material for lithium ion batteries, *ex-situ* characterizations indicate that these IF-MoS₂ hollow nanocages can provide large expandable spaces for volume change accompanied with the cycles. Such a highly desired structure offers remarkably improved lithium storage performance including high reversible capacity and good cycling behavior and high rate capability.

Introduction

Hollow-structured materials are of great interest for their electrochemical properties when used as electrodes in lithium ion batteries (LIBs) as a result of their unique structural features, stabilities and enhanced kinetics.[1-3] During the past several decades, various approaches have focused on different types of hollow structures fabricated using different synthesis routes, including the soft- or hard-template and the self-assembly template-free methods.[4-9] Most previous studies on preparing hollow-structured materials have focused on metal oxides, whereas the literature contains only a few reports of layered metal sulfides with intriguing hollow structures.[10, 11]

As a typical layered transition-metal sulfide, molybdenum disulfide (MoS₂) has a structure analogous to that of graphite and is formed by van der Waals stacking of covalently bonded S-Mo-S layers into a close-packed hexagonal lattice.[12-14] Being chemically and electronically active, MoS₂ has shown great potential for use in electronic devices and in electrocatalysis, sensor and energy-storage applications.[15-20] MoS₂ occurs in nature predominantly in the form of a two-dimensional layered structure; in recent years, ultrathin, few-layer, and single-layer MoS₂ structures have been extensively investigated.[21-25] Actually, in the early 1990s, after the discovery of C₆₀ (buckminsterfullerene) by Kroto *et al*. in 1985,[26] Tenne *et al*. first reported on transition-metal dichalcogenides MX₂ (X = Ti, Nb, Mo; X = S, Se) nanoparticles exhibiting layer-like structures, including MoS₂ and WS₂ nanoparticles, that can form closed-cage structures with polyhedral or nanotubular shapes.[27-29] These new materials received the generic name "inorganic fullerene-like structures," abbreviated "IF".[30, 31] Later, with the synthesis and characterization of MoS₂ and WS₂ fullerenes and nanotubes, inorganic fullerene-like materials began to constitute an important family of nanostructures with interesting properties and potential applications.[32-34]

However, previous reports on the synthesis of IF-MoS₂ or WS₂ describe hazardous or complicated routes, such as using H₂S as a heat treatment,[35] chemical vapor deposition (CVD),[36] and a seed-assisted solution route followed by annealing,[37] among others; the nature of these routes greatly restricts the development and applications of IF materials. Thus, the development of a new and facile synthesis method for IF materials is an important but underexplored topic.

Therefore, in this work, we present a facile process for the synthesis of hollow-structured IF-MoS₂ nanocages with a diameter of ~100 nm. The synthesis involves the facile reduction of (NH₄)₂MoS₄ in an *N*-methyl-2-pyrrolidone (NMP) solution by an N₂H₄ aqueous solution to obtain the hollow MoSₓ precursor under ambient pressure, followed by an annealing process at high temperatures to form the IF-MoS₂ nanocage. When used as an electrode material in LIB anodes, the proposed hollow IF-MoS₂ nanocages deliver a high reversible capacity and stable cycling performance.

Results and discussion

a. *Collaborative Innovation Center of Henan Province for Green Manufacturing of Fine Chemicals, School of Chemistry and Chemical Engineering, Henan Normal University, Xinxiang 453007, PR China. E-mail: czr_56@163.com*

b. *National Institute for Materials Science (NIMS), 1-1 Namiki, Tsukuba, Ibaraki, 305-0044, Japan. E-mail: chang.kun@nims.go.jp*

c. *Biomedical Research Institute, National Institute of Advanced Industrial Science and Technology (AIST), 1-1-1 Higashi, Tsukuba 305-8566, Japan.*
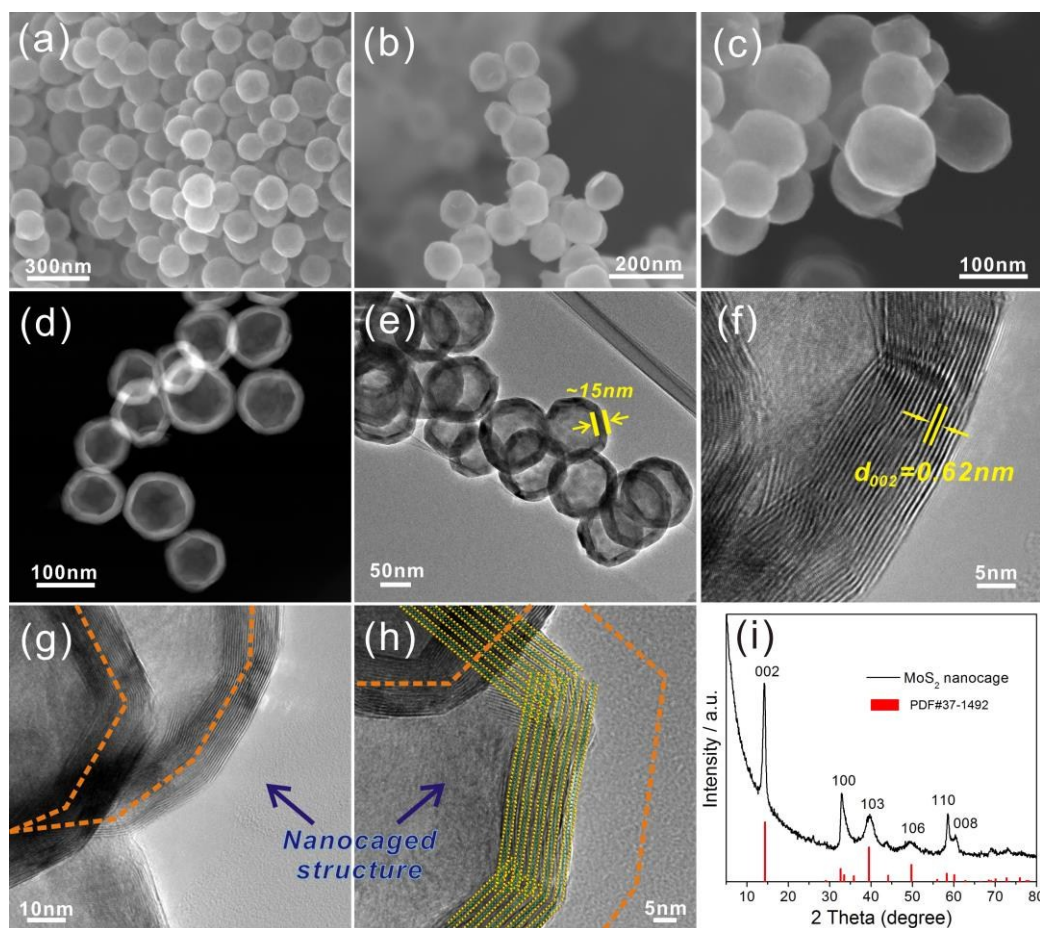
† These authors contributed equally

Figure 1. FESEM images (a-c) of the IF-MoS$_2$ nanocages at different magnifications, STEM (d) and TEM (e) images of the IF-MoS$_2$ nanostructure, HRTEM (f-h) images of the edges of the IF-MoS$_2$, and XRD (i) pattern of the IF-MoS$_2$ nanocages.

Characterization of Morphology and Structure

Figures 1a to 1c show the general views of the obtained MoS$_2$ nanoparticles at different magnifications. The proposed MoS$_2$ particles exhibit a uniform polyhedral structure with a relatively smooth surface and a diameter of ~100 nm. The STEM (Figure 1d) and TEM (Figure 1e) images indicate that the MoS$_2$ exhibits a hollow structure with a thickness of ~15 nm. Because the annealing was performed at 800°C for 2 h under N$_2$ gas protection, the MoS$_2$ shell exhibits a well-established layered structure with an interlayer distance of 0.62 nm (Figure 1f). The HRTEM images (Figure 1g and 1h) show that the MoS$_2$ shells actually consist of numerous nanosheets that spontaneously arise in the novel "close-edge" nanocages. The schematic of the microstructures of the MoS$_2$ in Figure 1h simulates the shell structure of an IF-MoS$_2$ nanocage. Figure 1i shows the XRD pattern, which indicates that the proposed MoS$_2$ is a typical hexagonal structure and is in accordance with the structure established by PDF card number 37-1492. The primary (002) diffraction peak appears at 2θ = 14.2°, with a d-spacing of

0.62 nm, indicating that the layered MoS$_2$ grows well along the c-axis, consistent with the measurement obtained from the HRTEM image in Figure 1f.

To determine the valence state of the elements, XPS measurements were carried out in the region from 0 to 1200 eV. As shown in Figure 2a, the signal of Mo and S atoms could be indexed clearly. Figure 2b shows a high-resolution Mo 3d spectrum, which contains the Mo 3d$_{3/2}$ and 3d$_{5/2}$ peaks at 232.38 eV and 229.24 eV, respectively, as the only two peaks, indicating the existence of only Mo(IV) in the compound. The peak at 226.40 eV is attributed to S 2s. Moreover, as shown in Figure 2c, the high-resolution S 2p spectrum contains the S 2p$_{1/2}$ peak at 163.20 eV and the S 2p$_{3/2}$ peak at 162.09 eV, indicating that the products are stoichiometric MoS$_2$. In addition, the EDX analysis of the products is shown in Figure S1. The calculated Mo-to-S atomic ratio is approximately 1:2.08, which is approaching the theoretical value for MoS$_2$.
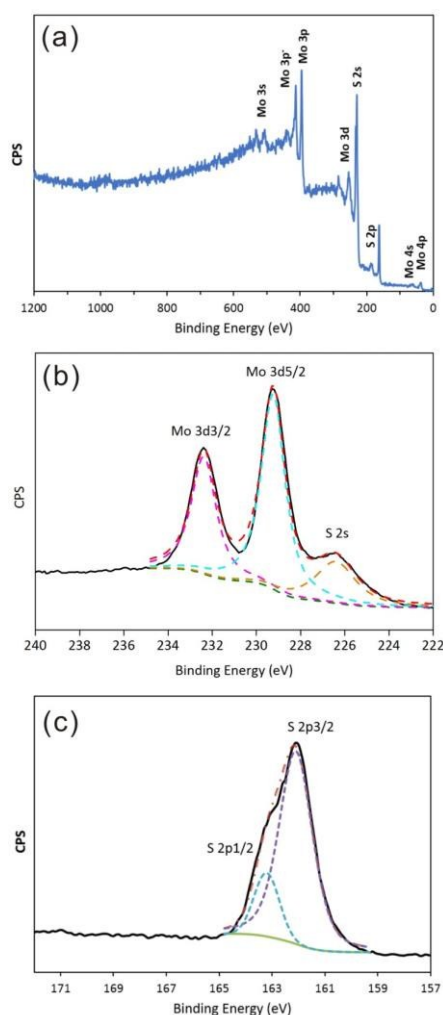
Analysis of Growth Mechanism

Figure 2. XPS spectrum of IF-MoS$_2$ nanocages after annealing at 800 °C for 2h under the N$_2$ atmosphere: (a)survey spectra, and high-resolution of (b) Mo 3d and (c) S 2p.

To determine the formation process for the hollow IF-MoS$_2$ nanocages, the as-prepared molybdenum sulfide precursors were characterized using FESEM and TEM prior to annealing, as shown in Figure 3. The precursor delivers uniform spherical nanoparticles with a diameter of ~150 nm (Figure 3a). The TEM images (Figures 3b and 3c) indicate a hollow structure with a shell thickness of ~20 nm. Compared with the size of the IF-MoS$_2$ nanocages shown in Figure 1, the diameter and shell thickness of the as-prepared MoS$_x$ precursor are significantly bigger, likely because of shrinkage during calcination. The HRTEM image (Figure 3d) of a partial enlargement of the shell indicates amorphous MoS$_x$ in the precursor. This amorphous character was also demonstrated in the XRD pattern, as no obvious diffraction peak was observed (see Figure S2). Therefore, the valence state of the MoS$_x$ precursor was analyzed by XPS; the resulting spectra are shown in Figure 4. Comparing with IF-MoS$_2$ material, two new strong XPS peaks of C$_{1s}$ and O$_{1s}$ are detected in the survey scan of Figure 4a. It might be attributed to impurity of unwashed NMP and carbon substrate of XPS test. After high temperature treatment, the impurity can be removed. As evident in Figure 4b, the high-resolution XPS spectrum of the Mo contains an
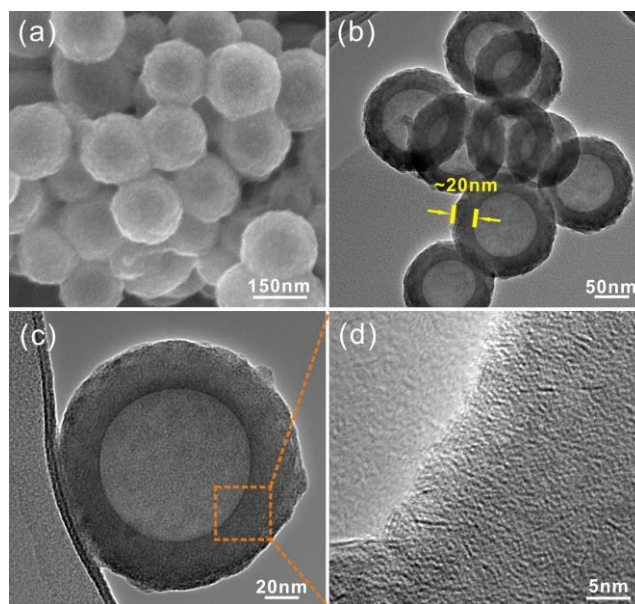

Figure 3. (a) FESEM image of the as-prepared MoS$_x$; (b and c) TEM images of the MoS$_x$; (d) HRTEM image of a partial enlargement of (c).

Mo 3d$_{3/2}$ peak at 231.80 eV and an Mo 3d$_{5/2}$ peak at 228.78 eV as two rough peaks; these peaks were deconvoluted into several fine peaks of Mo(IV), Mo(V) and Mo(VI), where the MoS$_x$ precursor did not reduce thoroughly during the solution-phase reaction. Moreover, in the XPS spectrum of the S (as shown in Figure 4c), with the exception of two peaks at 162.70 eV and 161.30 eV, which correspond to S 2p$_{1/2}$ and S 2p$_{3/2}$, other peaks are observed at approximately 168 eV. These peaks are attributed to S-N and S-O bonds, indicating that the precursor contains impurities. After the high-temperature treatment, the as-prepared MoS$_x$ precursor transforms into MoS$_2$.[38]

To illustrate the formation mechanism of the hollow-structured MoS$_x$ precursor, we conducted investigations using TEM to monitor the morphological evolution at different reaction stages. Figure 5a shows that the MoS$_x$ precursor, which exhibits an irregular and amorphous morphology, is produced at the beginning of the reaction. Upon close observation, the products contain a large amount of pores, which are attributable to the release of NH$_3$ gas produced during the reaction. As the reaction time increases, more (NH$_4$)$_2$MoS$_4$ is reduced, causing more NH$_3$ gas to be released, increasing the size of the pores. The MoS$_x$ precursor grows gradually around the NH$_3$ bubbles, which serve as a template. In Figures 5b and 5c, we observe that semi-finished hollow MoS$_x$ precursors with large pores form after 30 min and 1 h. When the reaction time increases to 2 h, as shown in Figure 3d, regions of the MoS$_x$ precursor are observed to form hollow spherical structures with non-closed edges. Increasing the reaction time to 5 h and 8 h, we find that the shell edges of the MoS$_x$ precursor close and that the hollow spheres become discernible (Figures 5e and 5f). On the basis of the aforementioned phenomenon, we conclude that the formation of the hollow structure of the MoS$_x$ precursor is caused
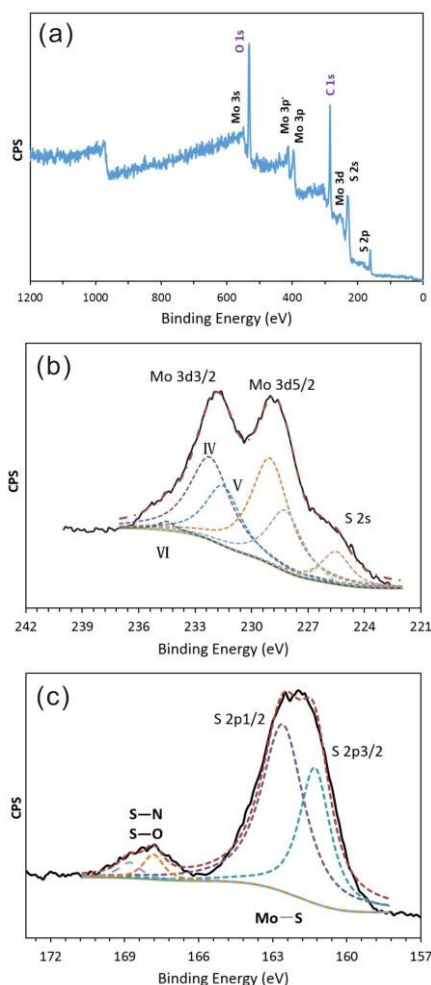
Figure 4. XPS spectrum of as-prepared MoS_x: (a)survey spectra, and high-resolution of (b) Mo 3d and (c) S 2p.

Figure 5. TEM images of the as-prepared MoS_x precursor at different reaction stages: (a) 5 min, (b) 30 min, (c) 1 h, (d) 2 h, (e) 5 h, and (f) 8 h (scale bars: 50 nm); (g) a schematic of the formation mechanism for the hollow MoS_x structure.

by the generation of NH_3 gas during the solution-phase reaction, which provides a bubble template for the growth of the MoS_x before being released to form the hollow structure. The formation mechanism is illustrated in Figure 5g. The selection of the reaction solvent is also important for preparing the hollow-structured MoS_x spheres. In this work, NMP was used as the solvent. However, water, ethanol and other solvents do not result in hollow-structured MoS_x spheres. The amorphous MoS_x in the hollow spherical precursor is recrystallized under the high temperatures and simultaneously reduced to layered MoS_2. Finally, hollow IF-MoS_2 nanocages are obtained after the high-temperature heat treatment.

Electrochemical Performance

To demonstrate the advantages of these hollow IF-MoS_2 nanocages, we investigated their electrochemical lithium storage properties as an anode material for LIBs and compared their performance to that of com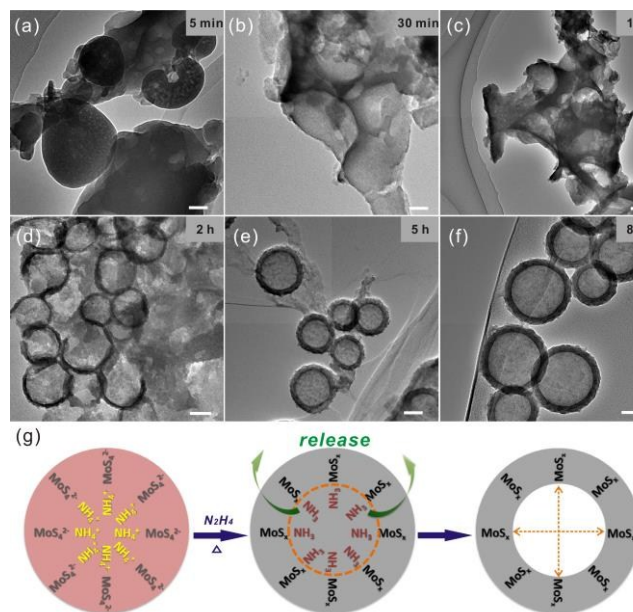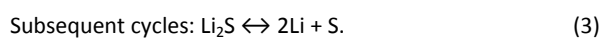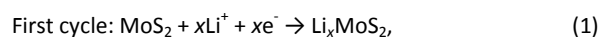mercial MoS_2. Figure 6 shows the electrochemical performance of the hollow IF-MoS_2 nanocage electrodes. The CV results for the proposed IF-MoS_2 nanocages (Figure 6a) are consistent with those for the commercial MoS_2 (Figure S3) and with previously reported data.[39-41] The first cycle shows two reduction peaks at approximately 0.8 and 0.4 V and one oxidation peak at approximately 2.3 V *vs*. Li/Li$^+$. The reduction peak at 0.8 V is attributed to Li insertion into the interlayers of MoS_2, accompanied by a phase transformation from the 2H to the 1T structure of Li_xMoS_2.[42] The second pronounced reduction peak is ascribed to the reduction of Li_xMoS_2 to metallic Mo and Li_2S via a conversion reaction, which is followed by the formation of a gel-like polymeric layer resulting from electrochemically driven electrolyte degradation.[43] The oxidation peak at 2.3 V is attributed to the delithiation of Li_2S: $Li_2S \rightarrow S + 2Li$.[41, 44] During the subsequent cathodic sweep, three other peaks appear at 2.0, 1.1 and 0.3 V. However, the peaks located at 0.8 and 0.4 V disappear, indicating that the lithiation and delithiation reaction of MoS_2 are irreversible processes. To further illustrate this fact, the *ex-situ* XRD analysis of IF-MoS_2 electrode was carried out after 100 cycles of charge and discharge (Figure S4). As shown in Figure S4, it can be seen that all the characteristic diffraction peaks of MoS_2 had disappeared indicating that the amorphous products are generated. According to a previous report,[45, 46] the lithium storage mechanism in MoS_2 can be expressed as:
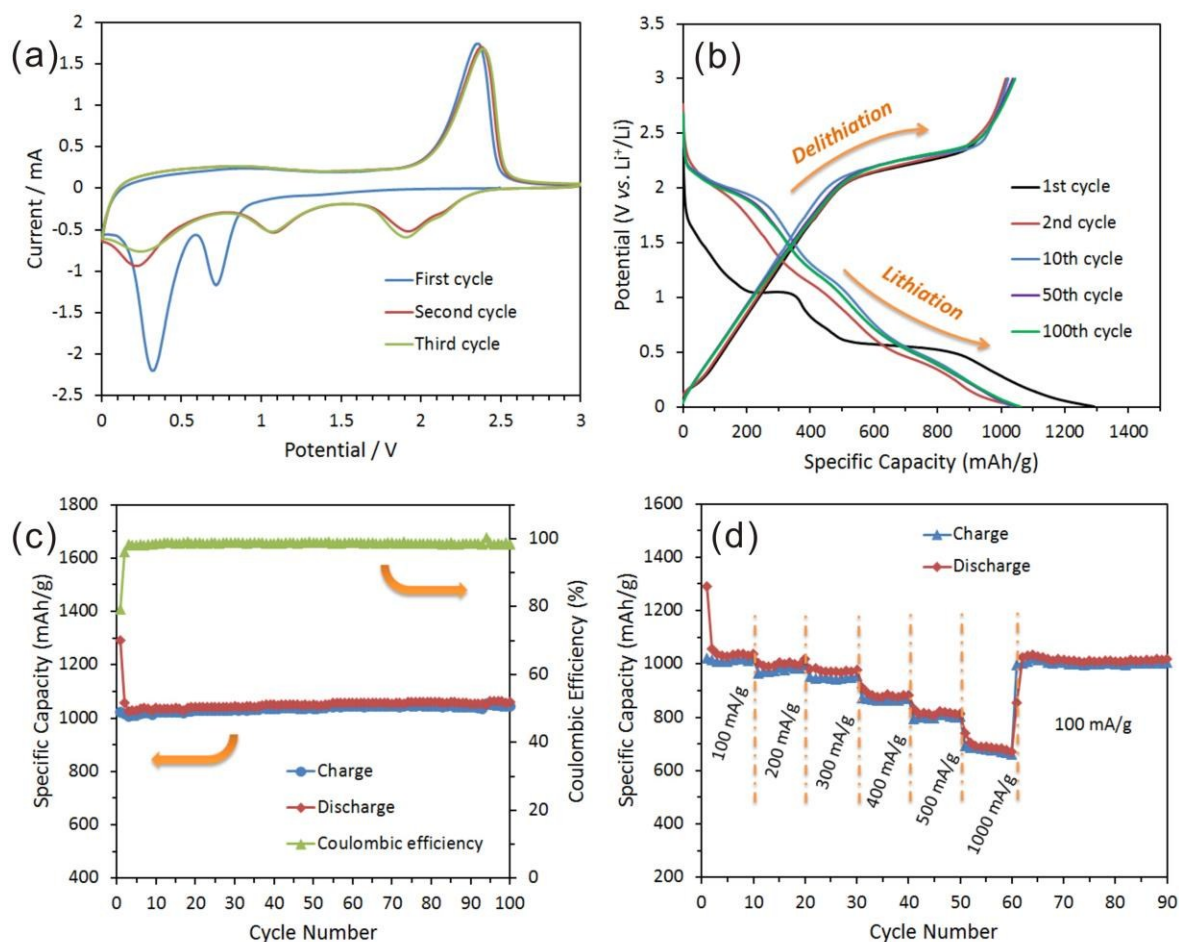
First cycle: $MoS_2 + xLi^+ + xe^- \rightarrow Li_xMoS_2$,   (1)

$Li_xMoS_2 + (4-x)Li^+ + (4-x)e^- \rightarrow Mo + 2Li_2S$,   (2)

Subsequent cycles: $Li_2S \leftrightarrow 2Li + S$.   (3)

ARTICLE

Figure 6. Electrochemical characterizations of a half-cell composed of an IF-MoS$_2$ nanocage electrode *vs*. Li foil: (a) cyclic voltammogram at a scan rate of 0.05 mV s^{-1} during the first three cycles, (b) the charge and discharge curves of the different cycles at a current density of 100 mAh g^{-1}, (c) cycling behavior of the electrode at a current density of 100 mAh g^{-1} and its corresponding Coulombic efficiency, (d) the cycling behavior of the electrode at various current densities.

Figure 6b shows the representative charge and discharge voltage profiles for the IF-MoS$_2$ nanocages at a current density of 100 mAh g^{-1} within a cut-off window of 0.005-3.0 V. Consistent with the CV results, the first discharge curve shows two major plateau regions at approximately 1.0 and 0.5 V *vs*. Li/Li$^+$; these results are approximately similar to those of the commercial MoS$_2$ (Figure S5) and also agree with the results reported for other well-crystallized MoS$_2$ electrodes.[44, 47] The initial discharge (lithiation) process leads to a very high specific capacity of 1289.7 mAh g^{-1}, which greatly exceeds the capacity of the commercial MoS$_2$, which has a capacity of 753.5 mAh g^{-1} (Figure S5). This high capacity of IF-MoS$_2$ nanocages might be related to their hollow structure, which provides more surface active sites for lithium storage.[3, 10] The IF-MoS$_2$ nanocage electrodes exhibit a high delithiation (charge) capacity of 1021.4 mAh g^{-1}, which corresponds to a small irreversible capacity loss of 20.8%. Generally, the initial capacity loss is caused mainly by the incomplete conversion reaction and by irreversible lithium loss due to the formation of a solid electrolyte interphase (SEI) layer, where the decomposition of the electrolyte on the surface of the MoS$_2$ forms a passivation layer on the

electrode.[48, 49] After the first cycle, the specific capacity of the IF-MoS$_2$ nanocage electrode stabilizes. All the subsequent cycles deliver an approximate overlap of the profiles associated with the lithiation and delithiation processes.

Figure 6c shows the cycling behavior and Coulombic efficiency of the IF-MoS$_2$ nanocage electrode. A comparison of the cycling stability of the commercial MoS$_2$ electrode (as shown in Figure S6) with that of the hollow-structured IF-MoS$_2$ nanocages reveals that the nanocages exhibit a more stable cycling life, where the reversible capacity is as high as 1043.7 mAh g^{-1} after 100 cycles. This good capacity retention is likely related to the hollow nanocage structure, which provides a robust "skeleton" to avoid structural damage to the electrode during the cycling process. By contrast, the cyclic stability of the commercial MoS$_2$ electrode (Figure S6) is so poor that the reversible capacity decreases from 632.4 mAh g^{-1} to 158.2 mAh g^{-1} after 75 cycles. In addition, the IF-MoS$_2$ nanocage electrode also exhibits a high initial Coulombic efficiency of 79.2%, which increases to almost 100% and after several cycles. Figure 6d shows the rate cycling behavior of the IF-MoS$_2$ nanocage electrode
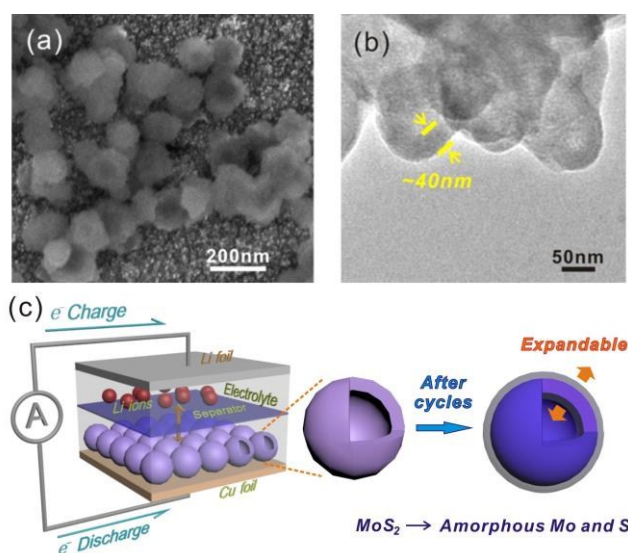
Figure 7. *Ex-situ* SEM (a) and TEM (b) images of IF-MoS$_2$ electrode after 100 cycles, (c) schematic illustration of IF-MoS$_2$ vs. Li half-cell, before and after cycles of IF-MoS$_2$ electrode.

material. The high reversible capacity and excellent cycling behavior of the IF-MoS$_2$ nanocages are reflected in their superior rate capability. The average specific capacities for the hollow IF-MoS$_2$ nanocages are 1008, 987, 945, 862, 796, and 680 mAh g^{-1} at current densities of 100, 200, 300, 400, 500, and 1000 mA g^{-1}, respectively. Remarkably, after cycling at 1000 mA g^{-1}, a stable capacity of ~1005 mAh g^{-1} is still delivered when the current density is reduced back to 100 mA g^{-1}, indicating high cycling stability.

In general capacity fading is caused by expansive volume excursions in the active electrode material during charging and discharging; leading to the pulverization of material and loss of electrical connectivity. The IF-MoS$_2$ electrode was therefore examined by *ex-situ* SEM and TEM after 100 cycles of charge and
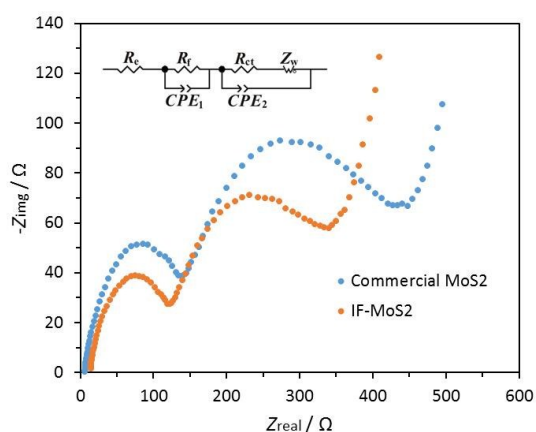

Figure 8. Nyquist plots of the commercial MoS$_2$ and IF-MoS$_2$ electrodes; the insert shows equivalent circuit model of the studied system, CPE represent the constant phase element, Z_{CPE} = {Q (jω)^n}$^{-1}$, 0 ≤ n ≤1.

Table 1. Impedance parameters derived using equivalent circuit model for commercial MoS$_2$ and IF-MoS$_2$.

Electrodes	R_e (Ω)	R_f (Ω)	Q_{CPE1} (μF)	R_{ct} (Ω)	Q_{CPE2} (μF)
c-MoS$_2$	8.6	206.9	33.1	117.8	98.1
IF-MoS$_2$	17.2	155.1	39.3	75.4	254.6

discharge (Figure 7). As shown in Figures 7a and 7b, it can be seen that after 100 cycles the morphology of IF-MoS$_2$ hollow structure is basically retained, whereas the nanocaged structure changes into nanosphere, indicating the formation of amorphous products after cycling, which is in aggreament with the *ex-situ* XRD analysis in Figure S4. Comparing with the Figure 1e, as shown in Figure 7b, it can be observed that the shell thickness of IF-MoS$_2$ increase from ~15 nm to ~40 nm. This fact indicates that a large volume change (~267%) of MoS$_2$-based materials is accompanied with the charge and discharge process. The reason why IF-MoS$_2$ electrode can exhibit the stable property is therefore schematically illustrated in Figure 7c. During the lithiation and delithiation process, MoS$_2$ was transferred into amorphous Mo and S which is simultaneously accompanied with a large volume change. The propused hollow-structured IF-MoS$_2$ electrode provides enough expandable space to avoid the damage of the electrode, so that it can deliver a good cycling stability and high rate capability. Figure 8 shows the electrochemical impedance spectrum (EIS) and the equivalent circuit model for both the IF-MoS$_2$ nanocage and commercial MoS$_2$ electrode materials. The kinetic differences in the IF-MoS$_2$ nanocage and the commercial MoS$_2$ electrode materials were further investigated by EIS modeling based on the modified equivalent circuit,[50] using the fitted impedance parameters listed in Table 1. In this model system, R_e represents the internal resistance of the test battery, R_f and CPE$_1$ are associated with the resistance and constant phase element of SEI film, R_{ct} and CPE$_2$ are associated with the charge-transfer resistance and constant phase element of the electrode/electrolyte interface, Z_w is associated with the Warburg impedance corresponding to the lithium-diffusion process. In Figure 8, the high frequency semicircle is corresponding to the resistance R_f and CPE$_1$ of SEI film, the semicircle in medium frequency region is assigned to the charge-transfer resistance R_{ct} and CPE$_2$ of electrode/electrolyte interface. The inclined line corresponds to the lithium-diffusion process within bulk of the electrode material. From the analysis results, it is known that the SEI film resistance R_f and charge-transfer resistance R_{ct} of the IF-MoS$_2$ nanocage electrode material are 155.1 and 75.4 Ω, respectively, which are significantly lower than those of the commercial MoS$_2$ (206.9 and 117.8 Ω). These results confirm that the hollow-nanocage structural MoS$_2$ can provide more active sites and greater electrolyte-electrode contact area for lithium ion insertion and extraction compared to the bulk MoS$_2$, indicating that this novel structural IF-MoS$_2$ nanocage is a promising anode material for high-performance LIBs used in a wide range of applications.

Conclusions

In summary, we have developed a new and facile strategy for the synthesis of hollow IF-MoS$_2$ nanocages with a uniform particle size of ~100 nm. This method first involves the synthesis of hollow MoS$_x$ spheres by a facile solution-phase route and subsequent annealing of the obtained precursors at 800°C for 2 h in an N$_2$ atmosphere. TEM images collected at different reaction steps revealed the formation mechanism of the MoS$_x$ hollow structural precursor, which is caused by the generation of NH$_3$ gas during the solution-phase reaction. This gas provides a bubble-like template for the growth of MoS$_x$ spheres and is subsequently released to form the hollow structures. After being annealed at a high temperature, the hollow MoS$_x$ precursor changes into hollow MoS$_2$ consisting of numerous nanosheets, which spontaneously appear in the novel "close-edge" nanocages. The IF-MoS$_2$ nanocages contain numerous active sites and exhibit a large electrolyte-electrode contact area and robust structure. As a result, when this material was evaluated as an anode material for LIBs, the hollow-structured IF-MoS$_2$ nanocage could provide a large expandable space for volume change accompanied with the cycles, and therefore exhibited not only a high reversible capacity but also a remarkably stable capacity retention for 100 cycles and an enhanced rate capability at current densities as high as 1000 mA g^{-1}.

Experimental

Synthesis of hollow IF-MoS$_2$ nanocages.

All chemical reagents used in this work were of analytical grade. First, 0.5 mmol of ammonium tetrathiomolybdate ((NH$_4$)$_2$MoS$_4$) was added to a 200 mL beaker with 80 mL of NMP. After being ultrasonicated for stirred for 3 h, the obtained clear solution was transferred into a 250 mL three-necked flask. Then, 5.0 mL of N$_2$H$_4$·H$_2$O was added to the flask dropwise under magnetic stirring. Afterwards, the flask was heated to 80°C in an oil bath and constantly stirred for 12 h under gentle reflux. After naturally cooling, the black-brown precipitates were collected by centrifugation at 8000 rpm, washed sequentially with ethanol and deionized (DI) water, and then dried in a vacuum chamber at 80°C overnight. The as-prepared MoS$_x$ was placed into a porcelain boat and kept in the center of a quartz tube placed inside a typical tubular furnace; the tube was then purged with nitrogen (N$_2$) for 20 min to remove oxygen. The porcelain boat was subsequently heated to 800°C at 5°C min^{-1} under nitrogen flowing at 100 mL min^{-1}. Two hours later, the furnace was allowed to cool to room temperature. The resulting black powder was used for further tests and characterization.

Characterization.

The samples were characterized using X-ray diffraction (XRD, RINT-2000, Rigaku Corp., Japan) with Cu-Kα$_1$ radiation, field-emission scanning electron microscopy (FESEM, Hitachi S-4800), transmission electron microscopy (TEM, TECNAI G2 F30, Japan), and energy-dispersive X-ray spectroscopy (EDX,

GENESIS 4000). The X-ray photoelectron spectroscopy (XPS) data were collected using a PHI Quantera SXM (ULVAC-PHI, Japan).

Electrochemical measurements.

The negative electrodes for the battery tests were composed of MoS$_2$, acetylene black, and polyvinylidene fluoride (PVDF) in a weight ratio of 75:10:15. The mixture of the active material, acetylene black and PVDF was ground for 2 h in an agate mortar. The mixture was then dried in a vacuum oven at 80°C for 4 h to remove any moisture. Afterwards, the NMP was injected to form a slurry, which was subsequently spread onto a copper foil with a thickness of 0.1 mm and a diameter of 12 mm, dried at 80°C in a drying oven for 2 h, compacted using a hydraulic press and then dried again at 120°C for 12 h in a vacuum drying chamber. Button cells (2025R) containing Li foil as a counter electrode, a polypropylene film (Celgard 2400) as a separator, and 1 M (mol L^{-1}) LiPF$_6$ in a mixture of ethylene carbonate/dimethyl carbonate/diethyl carbonate (EC/DMC/DEC 1:1:1 by volume) as an electrolyte were assembled in an argon-filled glovebox. Constant-current charge and discharge tests were performed on a cell test system (Land CT2001A) at potentials between 0.005 and 3.0 V. Cyclic voltammetry (CV) tests were carried out using an electrochemical workstation (CHI 660C) over a potential range from 0.005 to 3.0 V at a scan rate of 0.1 mV s^{-1}. Electrochemical impedance tests were also performed using an electrochemical workstation (CHI 660C) over the frequency range from 0.01 Hz to 100 kHz and at an amplitude of 5 mV.

Acknowledgements

References

1. X. W. Lou, L. A. Archer and Z. C. Yang, *Adv. Mater.*, 2008, **20**, 3987-4019.
2. L. F. Shen, L. Yu, X. Y. Yu, X. G. Zhang and X. W. Lou, *Angew. Chem. Int. Ed.*, 2015, **54**, 1868-1872.
3. Z. Y. Wang, L. Zhou and X. W. Lou, *Adv. Mater.*, 2012, **24**, 1903-1911.
4. J. B. Joo, Q. Zhang, I. Lee, M. Dahl, F. Zaera and Y. D. Yin, *Adv. Funct. Mater.*, 2012, **22**, 166-174.
5. J. H. Sun, J. S. Zhang, M. W. Zhang, M. Antonietti, X. Z. Fu and X. C. Wang, *Nat Commun*, 2012, **3**, 1139.
6. L. Yu, L. Zhang, H. B. Wu and X. W. Lou, *Angew. Chem. Int. Ed.*, 2014, **53**, 3711-3714.
7. H. Hu, B. Y. Guan, B. Y. Xia and X. W. Lou, *J. Am. Chem. Soc.*, 2015, **137**, 5590-5595.
8. L. F. Shen, L. Yu, H. B. Wu, X. Y. Yu, X. G. Zhang and X. W. Lou, *Nat Commun*, 2015, **6**, 6694.
9. L. N. Ye, C. Z. Wu, W. Guo and Y. Xie, *Chem. Commun.*, 2006, DOI: Doi 10.1039/B610601c, 4738-4740.

10. X. Y. Yu, H. Hu, Y. W. Wang, H. Y. Chen and X. W. Lou, *Angew. Chem. Int. Ed.*, 2015, **54**, 7395-7398.

11. M. Wang, G. D. Li, H. Y. Xu, Y. T. Qian and J. Yang, *ACS Appl. Mater. Interfaces*, 2013, **5**, 1003-1008.

12. B. Radisavljevic, A. Radenovic, J. Brivio, V. Giacometti and A. Kis, *Nat. Nanotechnol.*, 2011, **6**, 147-150.

13. S. S. Chou, Y. K. Huang, J. Kim, B. Kaehr, B. M. Foley, P. Lu, C. Dykstra, P. E. Hopkins, C. J. Brinker, J. X. Huang and V. P. Dravid, *J. Am. Chem. Soc.*, 2015, **137**, 1742-1745.

14. C. L. Tan and H. Zhang, *Chem. Soc. Rev.*, 2015, **44**, 2713-2731.

15. Y. G. Li, H. L. Wang, L. M. Xie, Y. Y. Liang, G. S. Hong and H. J. Dai, *J. Am. Chem. Soc.*, 2011, **133**, 7296-7299.

16. B. Mahler, V. Hoepfner, K. Liao and G. A. Ozin, *J. Am. Chem. Soc.*, 2014, **136**, 14121-14127.

17. M. A. Lukowski, A. S. Daniel, F. Meng, A. Forticaux, L. S. Li and S. Jin, *J. Am. Chem. Soc.*, 2013, **135**, 10274-10277.

18. Z. Hu, L. X. Wang, K. Zhang, J. B. Wang, F. Y. Cheng, Z. L. Tao and J. Chen, *Angew. Chem. Int. Ed.*, 2014, **53**, 12794-12798.

19. K. Chang and W. X. Chen, *ACS Nano*, 2011, **5**, 4720-4728.

20. H. J. Tang, J. Y. Wang, H. J. Yin, H. J. Zhao, D. Wang and Z. Y. Tang, *Adv. Mater.*, 2015, **27**, 1117-1123.

21. L. Cai, J. F. He, Q. H. Liu, T. Yao, L. Chen, W. S. Yan, F. C. Hu, Y. Jiang, Y. D. Zhao, T. D. Hu, Z. H. Sun and S. Q. Wei, *J. Am. Chem. Soc.*, 2015, **137**, 2622-2627.

22. Y. W. Tan, P. Liu, L. Y. Chen, W. T. Cong, Y. Ito, J. H. Han, X. W. Guo, Z. Tang, T. Fujita, A. Hirata and M. W. Chen, *Adv. Mater.*, 2014, **26**, 8023-8028.

23. J. Z. Chen, X. J. Wu, L. S. Yin, B. Li, X. Hong, Z. X. Fan, B. Chen, C. Xue and H. Zhang, *Angew. Chem. Int. Ed.*, 2015, **54**, 1210-1214.

24. K. Chang, D. S. Geng, X. F. Li, J. L. Yang, Y. J. Tang, M. Cai, R. Y. Li and X. L. Sun, *Adv Energy Mater*, 2013, **3**, 839-844.

25. Z. Y. Lu, W. Zhu, X. Y. Yu, H. C. Zhang, Y. J. Li, X. M. Sun, X. W. Wang, H. Wang, J. M. Wang, J. Luo, X. D. Lei and L. Jiang, *Adv. Mater.*, 2014, **26**, 2683-2687.

26. H. W. Kroto, J. R. Heath, S. C. Obrien, R. F. Curl and R. E. Smalley, *Nature*, 1985, **318**, 162-163.

27. R. Tenne, L. Margulis, M. Genut and G. Hodes, *Nature*, 1992, **360**, 444-446.

28. L. Margulis, G. Salitra, R. Tenne and M. Talianker, *Nature*, 1993, **365**, 113-114.

29. R. Rosentsveig, A. Margolin, A. Gorodnev, R. Popovitz-Biro, Y. Feldman, L. Rapoport, Y. Novema, G. Naveh and R. Tenne, *J. Mater. Chem.*, 2009, **19**, 4368-4374.

30. R. Tenne, *Nat. Nanotechnol.*, 2006, **1**, 103-111.

31. R. Tenne and C. N. R. Rao, *Philos T Roy Soc A*, 2004, **362**, 2099-2125.

32. J. Etzkorn, H. A. Therese, F. Rocker, N. Zink, U. Kolb and W. Tremel, *Adv. Mater.*, 2005, **17**, 2372-2375.

33. X. L. Li and Y. D. Li, *J. Phys. Chem. B*, 2004, **108**, 13893-13900.

34. J. Chen and F. Wu, *Appl Phys a-Mater*, 2004, **78**, 989-994.

35. A. Margolin, F. L. Deepak, R. Popovitz-Biro, M. Bar-Sadan, Y. Feldman and R. Tenne, *Nanotechnology*, 2008, **19**, 9.

36. X. L. Li, J. P. Ge and Y. D. Li, *Chemistry-a European Journal*, 2004, **10**, 6163-6171.

37. E. Blanco, D. Uzio, G. Berhault and P. Afanasiev, *J. Mater. Chem. A*, 2014, **2**, 3325-3331.

38. G. Alonso, M. Del Valle, J. Cruz, A. Licea-Claverie, V. Petranovskii and S. Fuentes, *Catal. Lett.*, 1998, **52**, 55-61.

39. L. Zhang and X. W. Lou, *Chemistry-a European Journal*, 2014, **20**, 5219-5223.

40. L. C. Yang, S. N. Wang, J. J. Mao, J. W. Deng, Q. S. Gao, Y. Tang and O. G. Schmidt, *Adv. Mater.*, 2013, **25**, 1180-1184.

41. H. Liu, D. W. Su, R. F. Zhou, B. Sun, G. X. Wang and S. Z. Qiao, *Adv Energy Mater*, 2012, **2**, 970-975.

42. K. Chang and W. X. Chen, *Chem. Commun.*, 2011, **47**, 4252-4254.

43. C. F. Zhang, Z. Y. Wang, Z. P. Guo and X. W. Lou, *ACS Appl. Mater. Interfaces*, 2012, **4**, 3765-3768.

44. F. Zhou, S. Xin, H. W. Liang, L. T. Song and S. H. Yu, *Angew. Chem. Int. Ed.*, 2014, **53**, 11552-11556.

45. X. P. Fang, C. X. Hua, X. W. Guo, Y. S. Hu, Z. X. Wang, X. P. Gao, F. Wu, J. Z. Wang and L. Q. Chen, *Electrochim. Acta*, 2012, **81**, 155-160.

46. Y. L. Liang, H. D. Yoo, Y. F. Li, J. Shuai, H. A. Calderon, F. C. R. Hernandez, L. C. Grabow and Y. Yao, *Nano Lett.*, 2015, **15**, 2194-2202.

47. Y. X. Wang, K. H. Seng, S. L. Chou, J. Z. Wang, Z. P. Guo, D. Wexler, H. K. Liu and S. X. Dou, *Chem. Commun.*, 2014, **50**, 10730-10733.

48. J. W. Zhou, J. Qin, X. Zhang, C. S. Shi, E. Z. Liu, J. J. Li, N. Q. Zhao and C. N. He, *ACS Nano*, 2015, **9**, 3837-3848.

49. S. Hu, W. Chen, J. Zhou, F. Yin, E. Uchaker, Q. F. Zhang and G. Z. Cao, *J. Mater. Chem. A*, 2014, **2**, 7862-7872.

50. S. B. Yang, H. H. Song and X. H. Chen, *Electrochem. Commun.*, 2006, **8**, 137-142.

Graphical abstract

MoS$_2$ nanocage anodes synthesized by bubble-template-assisted method can provide a

large expandable area to stabilize the electrode structure during cycling.